Direct measurement of the astrophysical ^{19}F$(p, \alpha\gamma)$ ^{16}O reaction in a deep-underground laboratory

L. Y. Zhang,[1,10] J. Su,[1,10] J. J. He,[1,10,*] R. J. deBoer,[2,†] D. Kahl,[3,‡] M. Wiescher,[2] D. Odell,[4] Y. J. Chen,[1] X. Y. Li,[1] J. G. Wang,[5] L. Zhang,[6] F. Q. Cao,[6] H. Zhang,[6] Z. C. Zhang,[7] T. Y. Jiao,[5] Y. D. Sheng,[1] L. H. Wang,[1] L. Y. Song,[1] X. Z. Jiang,[1] Z. M. Li,[1] E. T. Li,[7] S. Wang,[8] G. Lian,[6] Z. H. Li,[6] B. Guo,[6] X. D. Tang,[5] L. T. Sun,[5] Q. Wu,[5] J. Q. Li,[5] B. Q. Cui,[6] L. H. Chen,[6] R. G. Ma,[6] N. C. Qi,[9] W. L. Sun,[9] X. Y. Guo,[9] P. Zhang,[9] Y. H. Chen,[9] Y. Zhou,[9] J. F. Zhou,[9] J. R. He,[9] C. S. Shang,[9] M. C. Li,[9] J. P. Cheng,[1] and W. P. Liu[6]

[1]*Key Laboratory of Beam Technology of Ministry of Education, College of Nuclear Science and Technology, Beijing Normal University, Beijing 100875, China*

[2]*The Joint Institute for Nuclear Astrophysics, Department of Physics, University of Notre Dame, Notre Dame, Indiana 46556, USA*

[3]*Extreme Light Infrastructure - Nuclear Physics, Horia Hulubei National Institute for R&D in Physics and Nuclear Engineering (IFIN-HH), Bucharest-Măgurele 077125, Romania*

[4]*Institute of Nuclear and Particle Physics and Department of Physics and Astronomy, Ohio University, Athens, Ohio 45701, USA*

[5]*Institute of Modern Physics, Chinese Academy of Sciences, Lanzhou 730000, China*

[6]*China Institute of Atomic Energy, Beijing 102413, China*

[7]*College of Physics and Optoelectronic Engineering, Shenzhen University, Shenzhen 518060, China*

[8]*Shandong Provincial Key Laboratory of Optical Astronomy and Solar-Terrestrial Environment, Institute of Space Sciences, Shandong University, Weihai 264209, China*

[9]*Yalong River Hydropower Development Company, Chengdu 610051, China*

[10]*Institute of Radiation Technology, Beijing Academy of Science and Technology, Beijing 100875, China*

(Received 1 July 2022; accepted 13 October 2022; published 14 November 2022)

Fluorine is one of the most interesting elements in nuclear astrophysics. The ^{19}F(p, α) ^{16}O reaction is of astrophysical importance in addressing fluorine abundances in the universe and CNO material loss in the first generation stars. As a day-1 campaign in the Jinping Underground Nuclear Astrophysics experiment facility (JUNA), we report the full direct measurement results of the ^{19}F$(p, \alpha\gamma)$ ^{16}O reaction, which is one of the important channels in the ^{19}F(p, α) ^{16}O reaction. The γ-ray yields were measured over a center-of-mass energy range of $E_{\mathrm{c.m.}} = 72.4$–344 keV, covering the astrophysical Gamow window. The measurement has reached down to an unprecedentedly low energy of 72.4 keV. The experiment was performed under the extremely low cosmic-ray-induced background environment of the China JinPing underground Laboratory (CJPL), one of the deepest underground laboratories in the world (2400 m). The astrophysical S factors in the energy region of 72.4–188.8 keV have been derived experimentally for the first time. The present low-energy astrophysical S factors deviate significantly from previous theoretical predictions, and the associated uncertainties are remarkably reduced. The thermonuclear ^{19}F$(p, \alpha\gamma)$ ^{16}O rate has been determined down to a low temperature of $\approx$0.05 GK, for astrophysical modeling, based on a firmer experimental basis. Furthermore, the present work shows that the contribution owing to the (p, α_0) channel dominates the total (p, α) rate over the entire low temperature region below 0.12 GK, clarifying the role these two channels contributing to the total rate.

DOI: 10.1103/PhysRevC.106.055803

I. INTRODUCTION

The astrophysical origin of fluorine is puzzling. Fluorine is a monoisotopic element, and the stable nuclide ^{19}F is rather fragile—a curious and critically important point in nuclear astrophysics. ^{19}F is very sensitive to the physical conditions within stars. Therefore, fluorine is often used to probe nucleosynthesis scenarios [1]. Since ^{19}F has a limited number of atomic and molecular absorption lines in stellar spectra from which reliable abundances are derived, it makes the nucleosynthetic origin of ^{19}F the least understood of all the light elements [2].

Astrophysical model calculations and observational data have suggested several possible ^{19}F production sites [1,3]. Woosley and Haxton [4] proposed ^{19}F production in Type II core-collapse supernovae (SNe) by neutrino spallation on ^{20}Ne; Jorissen *et al.* [5] observed the ^{19}F overabundances (with respect to solar) in red giant stars and provided evidence for ^{19}F production during shell He burning in asymptotic giant branch (AGB) stars [6,7]; Meynet and Arnould [8] identified He burning in Wolf-Rayet stars. Kobayashi *et al.* [9] considered the neutrino-process nucleosynthesis as the major origin of ^{19}F in metal-deficient stars (type II and Ia

*Corresponding author: hejianjun@bnu.edu.cn
†Corresponding author: rdeboer1@nd.edu
‡Corresponding author: david.kahl@eli-np.ro

supernovae and hypernovae) and AGB stars. In addition, a signature of fluorine was observed in the spectra of Nova Mon 2012 [10]; however, classical novae seem to account for $\leqslant 1\%$ of its solar abundance [11]. Therefore, it remains an open question to what extent each candidate site may contribute to the solar-system and galactic fluorine, and a precise rate of the $^{19}\mathrm{F}(p,\alpha)^{16}\mathrm{O}$ reaction plays an essential role in its answer.

AGB stars were thought to be the major contributor to galactic fluorine production [5]. However, the astronomically observed fluorine overabundances cannot be explained using the current standard AGB models, and it seems that additional mixing effects should be involved, i.e., fluorine is produced in the He-rich intershell and carried to the surface via recurrent dredge-up episodes [12]. Palmerini *et al.* [13] analyzed the possible effect of such extra mixing within an AGB star, and investigated the impact of different rates of the $^{19}\mathrm{F}(p,\alpha)^{16}\mathrm{O}$ destruction reaction. They found that the surface abundance of $^{19}\mathrm{F}$ varied by up to 50% when changing the rate of this reaction by a factor of ≈ 2.

In addition, the most metal-poor stars observed in our Milky Way's halo today display the diluted nucleosynthetic signatures resulting from population III (Pop III) stars that preceded them [14]. Keller *et al.* [15] discovered one of the oldest known stars in the universe, SMSS0313-6708, and suggested that the hot CNO breakout during hydrogen burning is the source of calcium (Ca) production, reporting $[\mathrm{Ca/H}] = -7.2$. Pop III stars begin their lives with primordial big-bang composition and initiate hydrogen burning via *p*-*p* chains and then contract until the central temperature is high enough (≈ 0.1 GK) to ignite the 3α process, creating a small abundance of carbon [16], e.g., $X_{^{12}\mathrm{C}} \approx 10^{-9}$ to serve as a catalyst and initiate the CNO cycles. The stellar evolution simulations of Clarkson and Herwig [17] demonstrated that it is unlikely that such large amounts of Ca can be produced by hot CNO breakout. The predicted Ca abundance was between ≈ 0.8 and nearly 2 dex lower than required by observations of the most metal-poor stars. However, if the ratio of the $^{19}\mathrm{F}(p,\gamma)^{20}\mathrm{Ne}$ and the $^{19}\mathrm{F}(p,\alpha)^{16}\mathrm{O}$ reaction rates was a factor of ≈ 6 higher than that reported in the NACRE compilation [18], their model predictions could account for the observed Ca abundances in first generation stars, such as SMSS0313-6708.

Therefore, the $(p,\gamma)/(p,\alpha)$ rate ratio can provide an invaluable tool to diagnose how the first stars evolved and died, and has far-reaching implications on stellar modeling. Therefore, an accurate determination of both the $^{19}\mathrm{F}(p,\alpha)^{16}\mathrm{O}$ and $^{19}\mathrm{F}(p,\gamma)^{20}\mathrm{Ne}$ rates around 0.1 GK is extremely important for pinning down the origin of Ca made by Pop III stars, as well as validating the stellar evolution models.

The $^{19}\mathrm{F}(p,\alpha)^{16}\mathrm{O}$ reaction occurs via three types of channels, i.e., (p,α_0), (p,α_π) and $(p,\alpha\gamma)$, as shown in Fig. 1; second-order transitions are negligible [19]. The (p,α_π) channel provides less than a $\approx 10\%$ contribution at low temperatures ≈ 0.05 GK [20,21]; the $(p,\alpha\gamma)$ channel dominates at temperatures above 0.2 GK, while the (p,α_0) channel dominates at the lower temperatures below ≈ 0.15 GK [20,22]. However, recent studies have shown that the $(p,\alpha\gamma)$ channel could possibly dominate the total rate even below ≈ 0.05 GK [23,24], where a significantly enhanced reaction rate is possible, owing to the interference between a possible 11-keV resonance and the well-known 323-keV resonance. These theoretical predictions and extrapolations require a new measurement to clarify. Furthermore, the existence of this 11-keV [25–27] is still an open question, which needs high-precision experimental evidence.

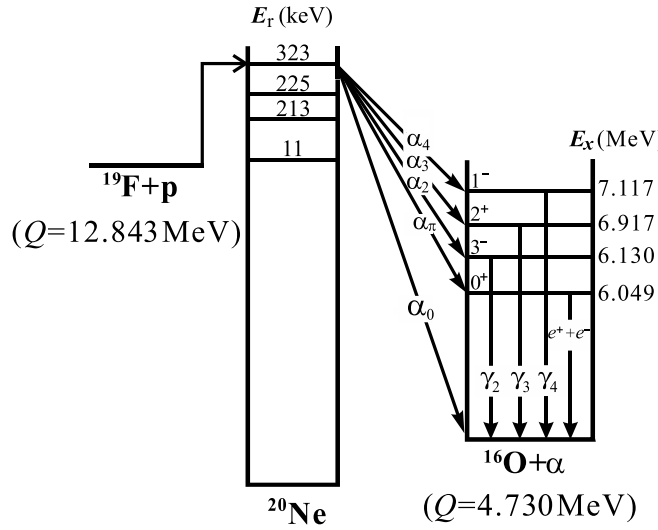

FIG. 1. Level scheme of the $^{19}\mathrm{F}(p,\alpha)^{16}\mathrm{O}$ reaction. The Q values are taken from AME2020 [36], four resonances are taken from Spyrou *et al.* [27], and nuclear structure data in $^{16}\mathrm{O}$ are taken from Kelley *et al.* [37].

So far, in the low temperature region, below ≈ 0.2 GK, the total thermonuclear $^{19}\mathrm{F}(p,\alpha)^{16}\mathrm{O}$ reaction rate is still not known precisely enough to address the fluorine overabundance phenomenon as well as the CNO material loss in Pop III stars. As for the temperature region (0.1–0.3 GK) of present astrophysical interest, the corresponding Gamow energy window is located in the range $E_{\mathrm{c.m.}} \approx 70$–$350$ keV (in the center-of-mass frame). Currently, the $(p,\alpha\gamma)$ and (p,α_0) channels have been measured, at above-ground laboratories, down to $E_{\mathrm{c.m.}} \approx 189$ [27] and 172 keV [28], respectively. In this work, we mainly focus on the $(p,\alpha\gamma)$ channel. Its cross section still needs to be measured in the energy region below 200 keV, although Couture *et al.* [29] obtained some resonance properties above $E_{\mathrm{c.m.}} = 200$ keV since then. Especially, in the low energy region, e.g., at ≈ 70 keV, the extrapolated cross sections still have uncertainties of up to several orders of magnitude [23,24,27]. However, the rate of cosmic-ray background radiation makes lower-energy direct measurements in laboratories at the Earth's surface (i.e., the above-ground laboratory) quite challenging.

China JinPing underground Laboratory (CJPL) [30], covered by about 2400 m of marble rock, is the deepest operational underground laboratory in the world. In this underground environment, the muon and neutron fluxes are reduced by 6 and 4 orders of magnitudes, respectively, compared to those at the Earth's surface. Owing to the depth advantage, the cosmic-ray induced background measured at CJPL [31] is significantly lower than that in LUNA (1400-m-thick dolomite rocks) [32]. With such a unique

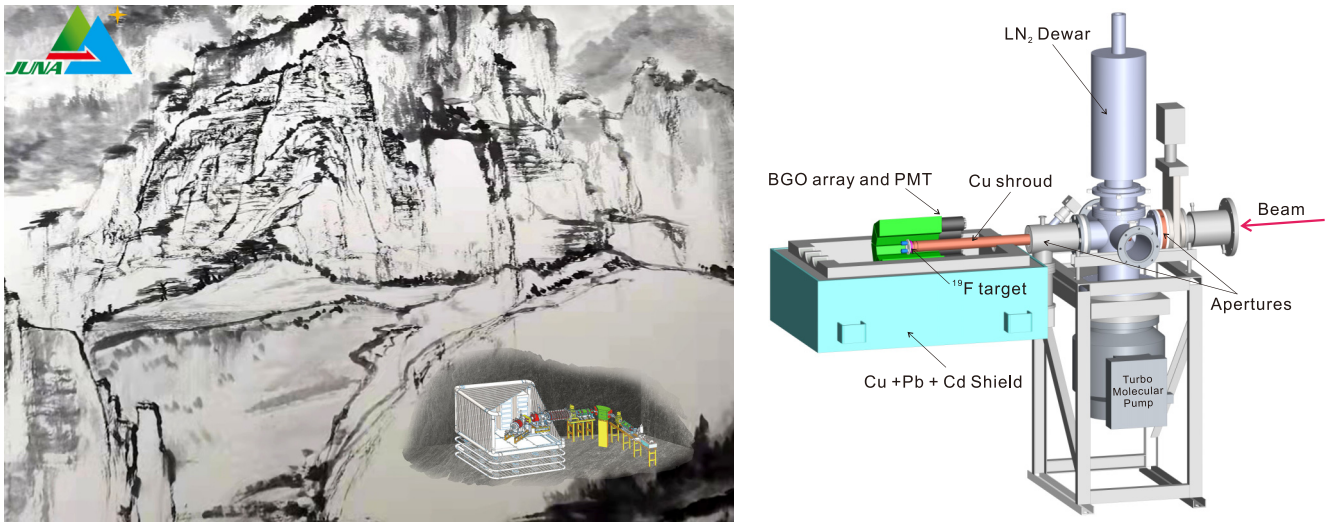

FIG. 2. Left panel: A combination of science and art rendition of the experimental site and platform for JUNA (credited to L.G. Chen for Chinese ink painting). Right panel: three-dimensional schematic view of the experimental setup.

superlow-background environment [33], the Jinping Underground Nuclear Astrophysics experiment facility (JUNA) project [34] was initiated in 2015. One of the subprojects [35] is dedicated to directly measuring the $^{19}\mathrm{F}(p,\alpha\gamma)^{16}\mathrm{O}$ reaction at Gamow energies.

In this paper, we will present the detailed results of a direct measurement of the $^{19}\mathrm{F}(p,\alpha\gamma)^{16}\mathrm{O}$ reaction at JUNA. The astrophysical S factors have been derived in the energy region of $E_{\mathrm{c.m.}} \approx 72.4$–$188.8$ keV. The unprecedentedly low energy measurements, extending down to 72.4 keV, directly cover the Gamow window. Our measurement decreases the uncertainty presented in the previous S-factor extrapolations [23,27] from orders of magnitude to the 10% level, which sets a solid experimental base for astrophysical modeling. Some brief results of this measurement were published elsewhere [38].

II. EXPERIMENT

The experiment was carried out on the high-current 400 kV JUNA accelerator at CJPL [39]. Figure 2 (left panel) shows an artistic rendition of the experimental site and platform for JUNA, and the setup details are shown in the right panel. A proton beam from the accelerator was collimated by two apertures of 10–20 mm diameter and then impinged on water-cooled targets, with a spot size of about 10 mm in diameter. For low energy measurements where higher intensity beam was required (for $E_p \leqslant 180$ keV, $I \approx 1$ mA), the beam was undulated periodicity over the target surface to reduce target damage. However, due to the limited space, the beam raster was not installed in the first-stage JUNA experiments. Alternatively, the beam was scanned by periodically changing the magnetic field of the beam deflector, installed about 3 m upstream from the target. In this way, the intense beam was spread over a rectangular area of about 4×4 cm^2. The uniformity of the beam scanning will be discussed later. For the $E_p > 180$ keV measurements, because the cross section becomes larger, the beam current was reduced to 1–10 μA, to reduce the detector dead time. In this case, it was unnecessary to use the beam scanning system. An inline Cu shroud, cooled to LN_2 (liquid nitrogen) temperature, extended close to the target to minimize carbon buildup on the target surface. There was no sign of carbon buildup upon visual inspection of all the targets during the experiment. Together with the target, the Cu shroud constituted the Faraday cup for charge integration of the beam. A negative voltage of 300 V was applied to the shroud to suppress secondary electrons from the target. The beam-current error was estimated to be 1%, mainly due to leakage current (typically <10 nA). Two very strong and durable implanted ^{19}F targets, developed in recent years [40,41], were utilized in this work. The targets were fabricated by implanting 50 keV ^{19}F ions into the 3-mm-thick Fe backings, and then sputtering about 50-nm-thick Cr foils to further prevent fluorine material loss.

A 4π bismuth germanate (BGO) detector array specially designed for the JUNA project [42], which has already been used and characterized in previous work (e.g., see Refs. [41,43]), was used to detect the γ rays. The BGO array was composed of eight identical segments with a length of 250 mm and a radial thickness of 63 mm, each covering a 45° azimuthal angle. For the 6130-keV γ rays of interest, the total absolute detection efficiency was ≈58%, with a ≈6% energy resolution achieved by alcohol-cooling the BGO crystals ($\approx -5\,^{\circ}$C). To suppress the natural γ-ray background emitted from the rocks and induced by the neutron capture reactions on the material around the detector (e.g., standers of the BGO detector and rocks, etc.), the BGO array was shielded by 5 mm copper, 100 mm lead, and 1 mm cadmium, respectively. Constant nitrogen gas flow was injected to the BGO array to eliminate radioactive Radon gas and avoid vapor build up on the cold BGO crystals.

Figure 3 shows a typical γ-ray spectrum taken at a proton beam energy of $E_p = 190$ keV with the 4π BGO array. Here, E_p denotes the proton beam energy before the Cr protective layer of the implanted fluorine target. Two background peaks, at 1460.8 keV (from ^{40}Ar) and 2614.5 keV (from ^{208}Tl),

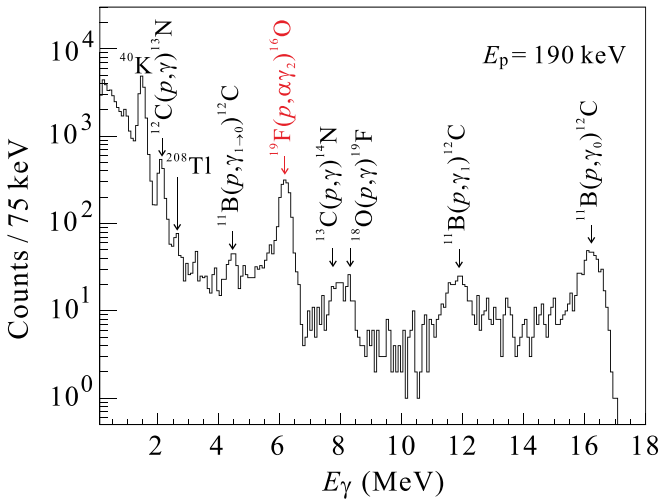

FIG. 3. Typical γ-ray spectrum measured at JUNA with a 4π BGO array at $E_p = 190$ keV. The 6130-keV γ-ray peak for the ^{19}F$(p,\alpha\gamma)\,^{16}$O reaction is indicated by the red text.

together with the 6130-keV peak from the ^{19}F$(p,\alpha\gamma_2)\,^{16}$O (i.e., from the α_2 channel) reaction were used for energy calibration. As for the 6130-keV γ rays, only the full energy peak was observed since the detection efficiency of the BGO array is quite high, and the single and double escape contributions are almost negligible. In addition, we also observed the γ rays induced by the ^{12}C and ^{13}C impurities from the target, as well as those induced by the ^{11}B contaminant mainly from the beam apertures, and their origins were analyzed in Ref. [41]. Some oxygen was introduced in the target during the target making process, especially ^{18}O$(p,\gamma)\,^{19}$F has relatively larger cross section than other stable oxygen isotopes, and that is why we observed the ^{18}O in the figure clearly. It should be mentioned that the ^{19}F$(p,\alpha\gamma)\,^{16}$O cross sections are so high that these background contributions to the 6130-keV γ rays of interested are negligible in the energy region of $E_p \geqslant$ 190 keV.

Figure 4 shows γ-ray spectra taken at six energy points below $E_p = 180$ keV. The contributions of the ^{19}F$(p,\alpha\gamma)\,^{16}$O reaction of interested and those contamination reactions have been simulated with a GEANT4 code [44] for each spectra, with their strengths adjusted to achieve the reasonable fits. It shows that almost all contamination have negligible influence on the aimed 6130-keV peak, except the ^{2}H contamination which became serious below ≈110 keV. The ^{18}O$(p,\gamma)\,^{19}$F peak becomes prominent close to its resonance around $E_p =$ 150 keV [45]. It should be noted that there is an unknown peak around 5.25 MeV, and hence one assumed peak (grey line) has been added to optimize the GEANT4 simulations. It shows that this assumed peak has only marginal effect on the 6130-keV peak and its contribution is considered in the uncertainties.

In this work, the ^{19}F$(p,\alpha\gamma)\,^{16}$O cross section was measured down to $E_p = 88$ keV (i.e., $E_{\rm c.m.} \approx 72.4$ keV), where the γ-ray spectrum was already given in Ref. [38]. Since the ^{19}F$(p,\alpha\gamma)\,^{16}$O cross section became extremely low, we got only a few counts in the region of interested (ROI) over the 6130-keV peak. In this case, the γ rays induced by the ^{2}H contamination became serious, and its tail probably contributes the ROI. The ^{2}H may have come from the ice on the cold shroud, since, when changing the target, some vapor may condense and freeze at the end of the cold shroud, which is very close to the target. This part of the shroud had some exposure to the air during the target changing process, even though this was mitigated by flowing nitrogen gas. This ice may have experienced bombardment by the scattered beam, thus introducing γ-ray backgrounds. Fortunately this will not influence the beam current measurement as the cold shroud was well grounded and insulated from the target. Moreover, it was unlikely that the ^{2}H came from the beam, as a 90-degree dipole was installed to eliminate beam contamination. To get a reliable background evaluation at this energy point, an experimental run with a pure Fe target (covered by a 50-nm-thick Cr layer) was done. Owing to the heavy ^{2}H contamination and limited beam time, a total net count of 30 ± 26 (with a very large uncertainty of about 80%) was obtained at this energy under the conditions of ≈1.0 mA average beam intensity and ≈2 days of machine time (a beam exposure of ≈190 C). Therefore, the energy of $E_{\rm c.m.} \approx 72.4$ keV can be seen as a lower limit accessible with the current JUNA setup. For future more precise measurements, the ^{2}H contamination must be reduced accordingly.

In addition, the α_3 and α_4 channel γ rays (6917 and 7117 keV) were also observed at $E_{\rm c.m.} > 200$ keV. The typical α_3 branching ratio is less than 0.7% in this energy region. The α_4 branching ratio is 2.8% for the $E_{\rm c.m.} = 323$ keV resonance and less than 0.6% for the nonresonant energy region.

Similarly to the previous test [41], the ^{19}F targets were monitored by observing the yield of the 6130-keV γ rays over the $E_{\rm c.m.} = 323$ keV resonance during the experimental runs. Figure 5 shows the experimental and GEANT4 simulated profiles of this resonance. For simplicity, the fluorine depth distribution was taken as uniform in the simulation and the thicknesses of Cr and F layers were varied to produce the best fit to the data. Due to the continuous beam bombardment, the Cr layer became thinner and the F atoms diffused into the target backing, resulting in a thicker F layer. The fluorine atom areal density is given by [46]

$$n = \frac{2A_Y}{\lambda^2 \omega\gamma\epsilon}, \tag{1}$$

where n is the F areal density, A_Y the integration over the 6130-keV peak in the γ-ray yield curve, λ the proton de Broglie wavelength, ϵ the BGO absolute detection efficiency of the 6130 keV γ ray, and $\omega\gamma$ the strength of the $E_{\rm c.m.} =$ 323 keV resonance, respectively. The F material loss was determined by comparing the A_Y value at different beam doses. A ≈4% fluctuation was observed in the A_Y values for both targets, and was taken as a systematical uncertainty of the yields. A possible source for such uncertainty was that the beam scanning was not ideally uniform. Target #1 had no obvious material loss under a total beam exposure of ≈69 C. Target #2 also exhibited no noticeable material loss under the first beam exposure of ≈70 C; however, for the lowest energy-point (i.e., at $E_{\rm c.m.} \approx 72.4$ keV) run, a ≈7% material loss was observed under another beam exposure of ≈200 C

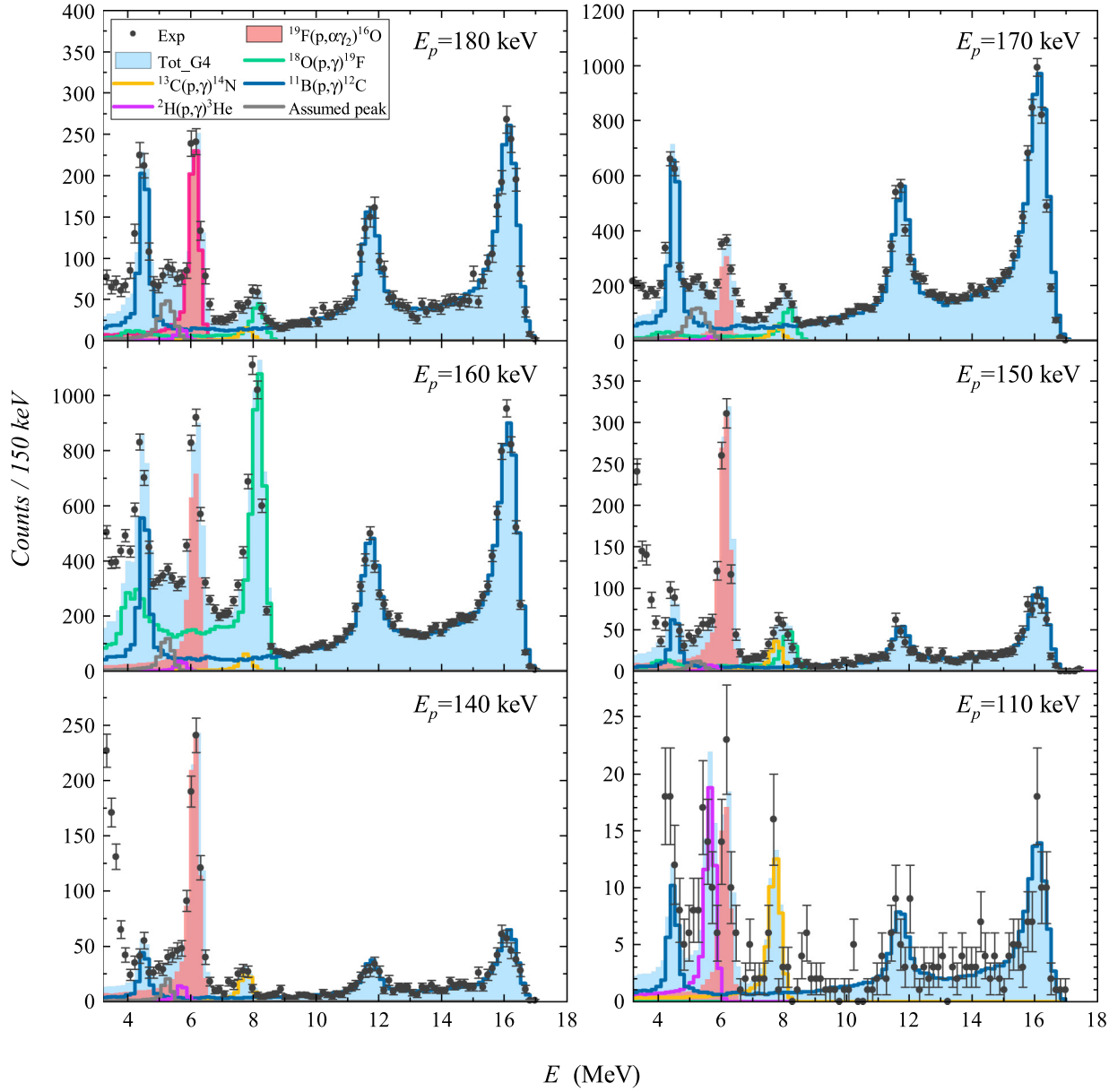

FIG. 4. γ-ray spectra measured with a 4π BGO array at six energy points (with statistical error only). Contributions from the $^{19}\mathrm{F}(p,\alpha\gamma)^{16}\mathrm{O}$ reaction and from the contaminant reactions are simulated with a GEANT4 code, with relevant strengths adjusted to reproduce the experimental data. Here, one assumed peak (indicated by the grey line) has been added to optimize the GEANT4 simulations for the unknown peak around 5.25 MeV. Note that the background below 4 MeV was not simulated, and hence it makes the experimental data much higher than the simulated ones at this energy region.

(totally ≈270 C on Target #2). Since this point has a 79.5% statistic error, this 7% target loss can be ignored.

Figure 6 shows the experimental yields for the $^{19}\mathrm{F}(p,\alpha\gamma)^{16}\mathrm{O}$ reaction measured at JUNA. The data for two targets (Target #1 and Target #2) are shown separately. The errors shown in the figure are statistical only and are less than 2% for most data points, while it is 87% for the lowest point at $E_{\mathrm{c.m.}} \approx 72.4$ keV.

For the $E_p \leqslant 180$ keV energy points, the beam scanning system was applied to reduce target deterioration. To determine its influence, the measurement at $E_p = 200$ keV was repeated several times with the beam scanning system on and off, and the yields were compared. The beam scanning system decreased the measured beam current by a factor of 1.09. This effect has been corrected for the data shown in Fig. 6, through iterative R-matrix calculations and GEANT4 simulations (see details in Sec. III).

Owing to the complicated target structure and the unknown self-sputtering rate during the implantation procedure, the absolute ^{19}F number density is hard to determine precisely. It is also very hard to get a precise, absolute, detection efficiency for the BGO detector. Therefore, we have made a relative measurement of the astrophysical S factors for the reaction studied. Here, the parameters of the ^{19}F depth distribution and

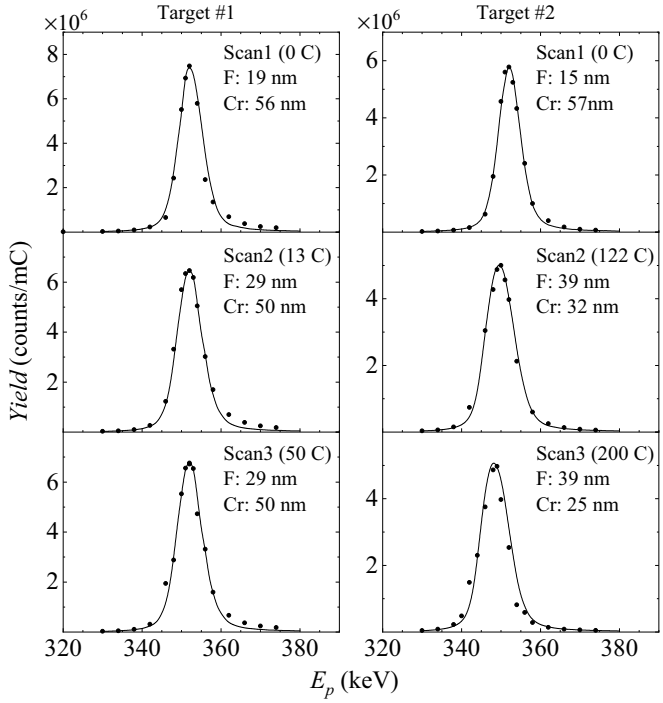

FIG. 5. Experimental and GEANT4 simulated yields of the $E_{\text{c.m.}} = 323$ keV resonance for two targets utilized in this experiment. For simplicity, the fluorine depth distribution was taken as uniform in the simulation, and the thicknesses of Cr and F layers were adjusted to achieve the best fits.

the Cr foil thickness were determined by adjusting their values in the GEANT4 simulation to reproduce the experimental yield over the 323-keV resonance. Thus, the product of absolute detection efficiency and ^{19}F number density was determined based on the well-known NACRE compilation's [18] strength value $\omega\gamma_{(p,\alpha\gamma)} = (23.1 \pm 0.9)$ eV (with an uncertainty of 3.9%) of the 323-keV resonance, which is a normalization factor [see Eq. (1)]. It should be noted that this NACRE strength is a weighted average of previous measurements, which includes both statistical and systematic errors. In fact, the most precise result was determined by Becker *et al.* [47], (although Couture *et al.* [29] made a new measurement later, but with larger uncertainty.) With these parameters, the effective beam energies and S factors for these off-resonance points were determined by the GEANT4 simulations as shown in Fig. 7. The uncertainties of the derived S factors mainly include three contributions: (1) the yield uncertainty as mentioned above; (2) a 5% uncertainty estimated for the GEANT4 simulation by assuming a 0.5 keV uncertainty in the reconstructed $E_{\text{c.m.}}$ value; and (3) a 3.9% uncertainty for the 323-keV resonance strength (from the normalization). For the energy points near or on the resonance peaks, the corresponding S factors were nonconstant over each energy point and cannot be determined precisely. Their yields can be reproduced well by using the known strength values for three resonances at $E_{\text{c.m.}} = 211$, 225, and 323 keV, verifying the present experimental method and analysis procedure. Numeric samples of the S factors and cross sections, as well as the associated uncertainties in the off-resonance region, are tabulated in Table I [38].

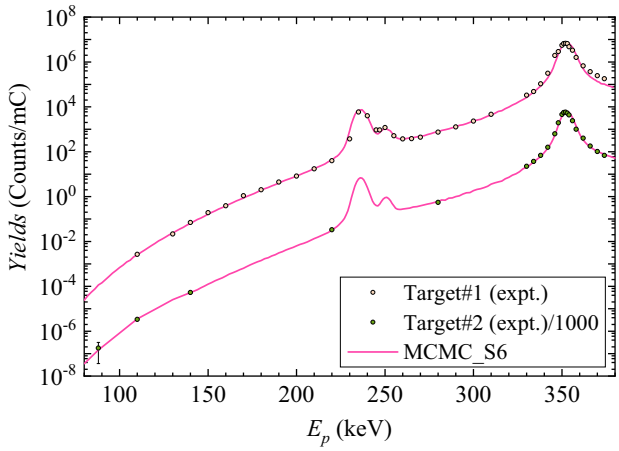

FIG. 6. Experimental yields for the $^{19}\text{F}(p,\alpha\gamma)\,^{16}\text{O}$ reaction measured by the JUNA experiment [38]. The results for two implanted targets are shown separately, where the Target #2 data are scaled down by a factor of 1000. The GEANT4 simulated curves are indicated for each target, based on the R-matrix Markov chain Monte Carlo (MCMC) fits (where S6 corresponds to a 50% quantile). Here the errors are statistical only, and, for some data points, the error bars do not exceed the size of the data points. See text for details.

III. *R*-MATRIX ANALYSIS

A multilevel multichannel R-matrix analysis, using the code AZURE2 [48,49], was used to fit the low energy $^{19}\text{F}(p,\alpha\gamma)\,^{16}\text{O}$ data, as well as previous higher energy data from the literature. At these low energies, the $^{19}\text{F}(p,\alpha\gamma)\,^{16}\text{O}$ reaction is populated almost exclusively through the $^{19}\text{F}(p,\alpha_2)\,^{16}\text{O}$ transition. The R-matrix fit to the higher energy data proved to be consistent with the previous analysis of deBoer *et al.* [23], therefore only the low energy part of the fit that overlaps with the present data are discussed here. To avoid the computationally intensive calculations needed to convolute the experimental yields in the region of narrow resonances with experimental resolution effects in the present analysis, the formalism of Brune [50] was used to fix values of the partial widths of the narrow resonances as described in Sec. II.

One of the main sources of uncertainty at low energies is the interference between the near threshold, possible subthreshold, and the higher lying resonances. In particular, the resonances with corresponding level spin-parities of 1^+ are currently thought to be the chief contributors over most of the low energy range of the cross section [38]. The present measurements, which extend to energies considerably lower than any made previously, rule out the majority of the different interference possibilities described in [23]. The three fit scenarios that were found to be the most compatible with the present data have been shown in Fig. 4 in Ref. [38]. They gave substantially different low energy S factors compared to the previous extrapolations made by Spyrou *et al.* [27]. This indicates the many sources of uncertainty in the previous extrapolations, stemming from the large uncertainties associated

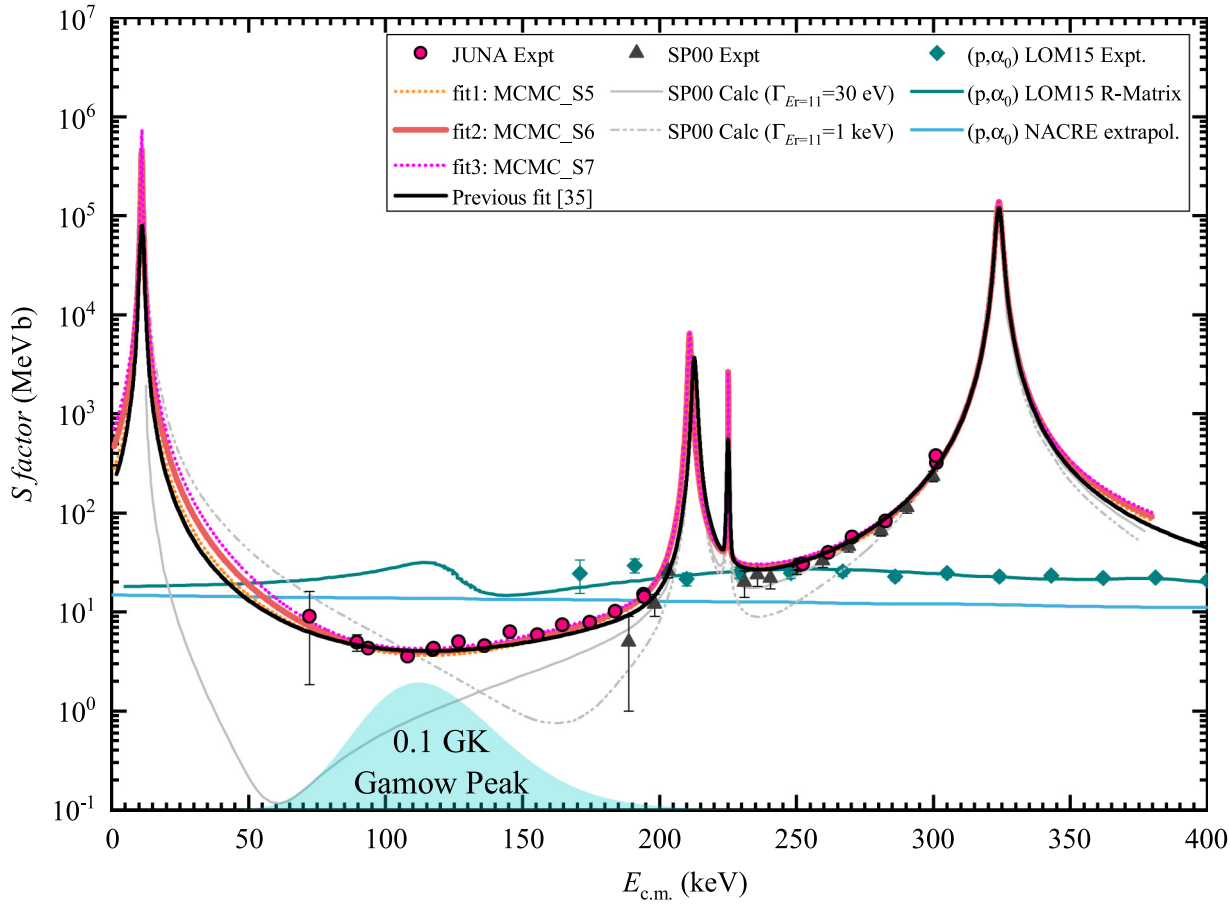

FIG. 7. Astrophysical S factors of the $^{19}\mathrm{F}(p,\alpha\gamma)^{16}\mathrm{O}$ reaction derived from the JUNA experiment (with statistical uncertainties only) [38]. Three R-matrix MCMC fits are shown, where S5, S6, and S7 correspond to the 16%, 50%, and 84% quantiles, respectively. The underlying distributions are approximately Gaussian in shape, so these would correspond to approximately 1σ uncertainty bands. The previous experimental data ("SP00 Expt") [27] and theoretical predictions ("SP00 Calc") [23,27] are shown for comparison. In contrast, our previous general R-matrix fit [38] is shown by the black sold line (labeled as "Previous fit"). As for the (p,α_0) channel, both the experimental data and R-matrix curve of LOM15 [28], as well as that of NACRE's simple extrapolation [18], are shown for comparison. The Gamow peak at 0.1 GK is shown schematically by the shaded region. See text for details.

with the level properties of the near threshold, and possible subthreshold resonances.

It was found that an accurate reproduction of the new experimental data could be achieved with contributions from the 1^+ near threshold resonance [25,27], a 1^+ subthreshold resonance, and the broad 2^+ level at $E_x = 13.095$ MeV, in addition to the tail contributions of the higher lying resonances determined from the previous analysis of deBoer *et al.* [23]. A poorer reproduction of the experimental data was possible with either a subthreshold state or near threshold resonance contribution, but the reproduction of the data was significantly improved when both contributions and the broad 2^+ state were included [38]. It is particularly noteworthy that the present data are the first direct measurements that indicate the presence of the near threshold resonance. It should also be noted that, due to the high level density and incomplete knowledge of the level structure of the ^{20}Ne compound system over this energy region, the R-matrix fit solution is not unique.

In order to quantify the significance of the different level contributions to the R-matrix fit, a Bayesian uncertainty analysis was performed using the Python package BRICK [51]. BRICK acts as a mediator, allowing communication between the Python MCMC sampler EMCEE [52] and the C++ R-matrix code AZURE2. As the MCMC calculations are computationally intensive, only the parameters associated with the three underlying resonance contributions with the largest uncertainties are explored. For the subthreshold resonance, the proton asymptotic normalization coefficient (ANC) is fixed to a value close to its Wigner limit, which is still consistent with low energy scattering data [23]. Finally, for the broad resonance corresponding to the 2^+ level, to simplify the calculation, Γ_{α_2} is set equal to the literature value of the total width, while Γ_p is given a wide uniform prior. Note that in the case of the 2^+ level that $\Gamma_{\alpha_2} \gg \Gamma_p$. In addition, the overall normalization was given a Gaussian prior of 10% uncertainty, which was returned as the posterior as expected. Table II details the fixed parameters and those allowed to vary along with the resulting uncertainties.

It is interesting to note that some rather different central values were obtained between the χ^2 fit (see Table I in Ref. [38]) and the maximum likelihood MCMC analysis (see Table II in this work). This is a reflection of the large

TABLE I. Experimental astrophysical S factors and cross sections for $^{19}\mathrm{F}(p,\alpha\gamma)\,^{16}\mathrm{O}$ derived for the nonresonant region (as shown in Fig. 7). The total uncertainties are listed in the parentheses, and the statistical uncertainties are listed in the last column. The overall systematical uncertainty of ≈7.4% was estimated.

$E_{\mathrm{c.m.}}$ (keV)	S factor (MeV b)	σ (b)	Stat. err. (%)
72.4	8.98(7.10)	$1.08(0.85)\times10^{-12}$	79.5
89.7	4.91(1.01)	$1.28(0.26)\times10^{-11}$	18.9
93.8	4.31(0.44)	$2.05(0.21)\times10^{-11}$	7.8
108.2	3.55(0.39)	$1.04(0.11)\times10^{-10}$	5.1
117.2	4.15(0.35)	$3.16(0.27)\times10^{-10}$	3.9
117.5	4.29(0.38)	$3.38(0.30)\times10^{-10}$	3.8
126.7	4.96(0.50)	$9.28(0.94)\times10^{-10}$	4.7
136.2	4.57(0.42)	$1.88(0.17)\times10^{-9}$	2.1
145.5	6.32(0.64)	$5.26(0.53)\times10^{-9}$	4.7
155.5	5.85(0.59)	$9.64(0.97)\times10^{-9}$	4.5
164.6	7.40(0.57)	$2.14(0.17)\times10^{-8}$	2.3
174.5	7.84(0.62)	$3.96(0.31)\times10^{-8}$	2.7
183.9	10.12(0.79)	$8.31(0.65)\times10^{-8}$	2.7
194.3	14.93(1.14)	$2.01(0.15)\times10^{-7}$	1.2
194.5	14.10(1.10)	$1.92(0.15)\times10^{-7}$	2.5
251.0	29.87(2.29)	$3.35(0.26)\times10^{-6}$	1.3
252.4	30.49(2.28)	$3.58(0.27)\times10^{-6}$	1.3
261.6	39.78(2.95)	$6.11(0.45)\times10^{-6}$	0.6
270.4	56.70(4.20)	$1.11(0.08)\times10^{-5}$	0.6
282.6	82.74(6.12)	$2.25(0.17)\times10^{-5}$	0.4
300.9	377.2(27.9)	$1.59(0.12)\times10^{-4}$	0.2
301.1	320.1(24.2)	$1.36(0.10)\times10^{-4}$	0.4

uncertainties obtained for the resonance parameters and the large degree of correlation between them, which leads to shallow minima in χ^2. A corner plot showing a posterior probability distributions from the MCMC analysis is drawn in Fig. 8. As expected, strong correlations are observed between the Γ_{α_2} widths of the subthreshold and near threshold states.

As for the three most probable R-matrix fits given in Fig. 4 in Ref. [38], although they exhibited quite different trends below the lowest energy data point achieved, the present JUNA experimental data already covered the full Gamow energy range of the current astrophysical interest. Therefore, the uncertainty in the present S-factor curve over the range of astrophysical interest has been greatly reduced compared to extrapolations based on previous higher energy measurements [23,24] (see Fig. 7). In addition, the extrapolations from Spyrou *et al.* [27] are also shown for comparison (two grey lines, labeled as SP00).

IV. ASTROPHYSICAL REACTION RATE

The thermonuclear $^{19}\mathrm{F}(p,\alpha\gamma)\,^{16}\mathrm{O}$ reaction rate has been calculated by numerical integration of the S factors in Fig. 7 with the well-known formula for $N_A\langle\sigma v\rangle$ given in Rolfs and Rodney [54],

$$N_A\langle\sigma v\rangle = N_A\sqrt{\frac{8}{\pi\mu}}\frac{1}{(kT)^{\frac{3}{2}}}\int_0^\infty S(E)\exp\left[-\frac{E}{kT}-2\pi\eta\right]dE, \tag{2}$$

where N_A is Avogadro's number, k is the Boltzmann constant, T is the temperature, μ is the reduced mass, and η is the Sommerfeld parameter.

At each temperature point, three reaction rates were given based on the three S-factor curves shown in Fig. 7. The maximum and minimum of the three rates were adopted as the high and low limits, the average of the maximum and minimum was adopted as the recommended median rate. In this way, the present median rate and the associated uncertainties are obtained over a temperature region of 0.005–1 GK, and are given in Table III. The present median rate can be parametrized by the standard format of Ref. [55],

$$\begin{aligned}
N_A\langle\sigma v\rangle_{(p,\alpha\gamma)} = {} & \exp\left(220.42-\frac{5.89736}{T_9}-\frac{241.877}{T_9^{1/3}}-278.432T_9^{1/3}+596.28T_9-310.853T_9^{5/3}-177.227\ln T_9\right)\\
& +\exp\left(-257.718-\frac{6.96149}{T_9}+\frac{234.148}{T_9^{1/3}}+180.172T_9^{1/3}-202.205T_9+63.9643T_9^{5/3}+110.693\ln T_9\right)\\
& +\exp\left(-38.5399+\frac{0.0640641}{T_9}-\frac{31.3093}{T_9^{1/3}}+80.6092T_9^{1/3}+18.9689T_9-19.2284T_9^{5/3}-23.4371\ln T_9\right)\\
& +\exp\left(-135.944-\frac{0.213409}{T_9}+\frac{4.14544}{T_9^{1/3}}-238.22T_9^{1/3}+5836.64T_9-24560.5T_9^{5/3}-18.7326\ln T_9\right),
\end{aligned}$$

with a fitting error of less than 1% over the temperature region of 0.005–1 GK. Above 1 GK, the NACRE [18] rate should be adopted.

In our previous work [38], a general R-matrix analysis was performed, while we have performed a more complicated R-matrix MCMC analysis in this work. Figure 9 shows the comparison between our present rate and our previous rate [38] (labeled as "Zhang *et al.*"). The present rate is higher than our previous ones below 0.1 GK is due to our new MCMC R-matrix analysis giving a higher S factor below

TABLE II. Summary of parameters and uncertainties determined from the MCMC analysis. The sign of the partial width indicates the sign of the corresponding reduced width amplitude. For the ^{20}Ne system, $S_p = 12.844$ MeV and $S_{\alpha_2} = 10.860$ MeV; above the separation energy partial widths are given, below ANCs are given.

$E_{\text{c.m.}}$	E_x		Γ_{α_0}	Γ_{α_2}
(keV)	(MeV)	J^π	($\text{fm}^{-1/2}$ or eV)	
−448	(12.396)[a]	1^+	(15)[a]	62^{+41}_{-30}
11	(12.855)[a]	1^+	(1.14×10^{-28})[a]	-600^{+230}_{-280}
251	(13.095)[a]	2^+	$-0.0144^{+0.0029}_{-0.0024}$	(1.62×10^{5})[a]

[a]Fixed.

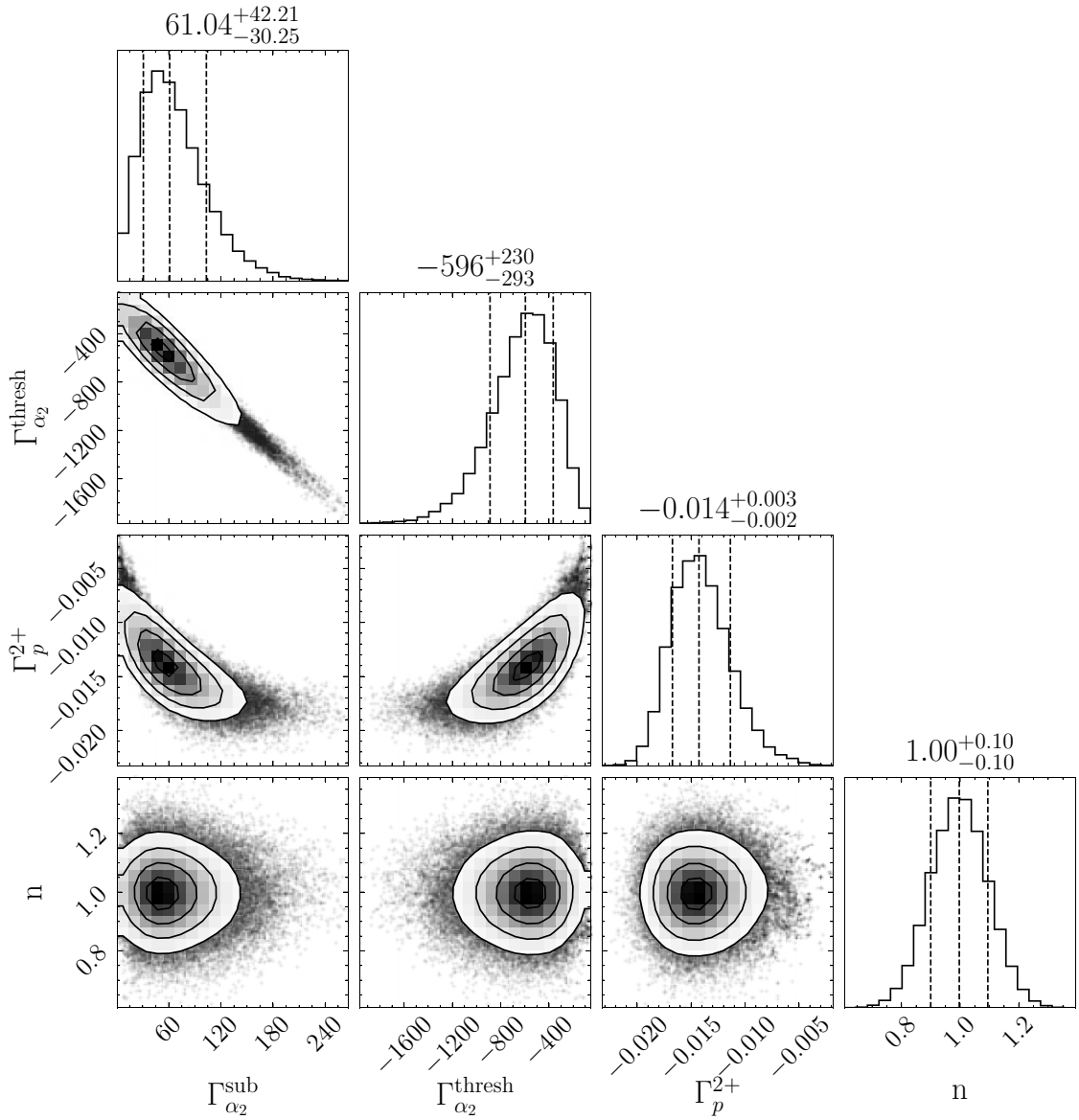

FIG. 8. Corner plot [53] of the posterior probability distributions calculated from the MCMC *R*-matrix uncertainty analysis for the partial widths, in units of eV, varied in the fitting. Note that the signs of the partial width reflect those of the corresponding reduced width amplitudes. The vertical dashed lines indicate the 16% (S5), 50% (S6), and 84% (S7) quantiles. Here *n* refers to the normalization factor for the $^{19}\text{F}(p,\alpha\gamma)^{20}\text{Ne}$ data.

TABLE III. Thermonuclear rate of $^{19}\mathrm{F}(p,\alpha\gamma)^{16}\mathrm{O}$ in units of $\mathrm{cm}^3\mathrm{s}^{-1}\,\mathrm{mol}^{-1}$.

T_9	Median rate	Low rate	High rate
0.005	4.86×10^{-31}	3.08×10^{-31}	7.11×10^{-31}
0.006	5.75×10^{-29}	3.65×10^{-29}	8.37×10^{-29}
0.007	3.11×10^{-27}	1.99×10^{-27}	4.51×10^{-27}
0.008	9.87×10^{-26}	6.35×10^{-26}	1.42×10^{-25}
0.009	1.98×10^{-24}	1.29×10^{-24}	2.83×10^{-24}
0.010	2.71×10^{-23}	1.78×10^{-23}	3.85×10^{-23}
0.015	3.02×10^{-19}	2.06×10^{-19}	4.20×10^{-19}
0.020	1.09×10^{-16}	7.65×10^{-17}	1.47×10^{-16}
0.025	7.05×10^{-15}	5.16×10^{-15}	9.25×10^{-15}
0.030	1.68×10^{-13}	1.29×10^{-13}	2.16×10^{-13}
0.035	2.10×10^{-12}	1.66×10^{-12}	2.66×10^{-12}
0.040	1.68×10^{-11}	1.37×10^{-11}	2.07×10^{-11}
0.045	9.82×10^{-11}	8.14×10^{-11}	1.17×10^{-10}
0.050	4.51×10^{-10}	3.81×10^{-10}	5.25×10^{-10}
0.055	1.72×10^{-9}	1.48×10^{-9}	1.97×10^{-9}
0.060	5.66×10^{-9}	4.95×10^{-9}	6.40×10^{-9}
0.065	1.65×10^{-8}	1.46×10^{-8}	1.85×10^{-8}
0.070	4.38×10^{-8}	3.91×10^{-8}	4.87×10^{-8}
0.075	1.07×10^{-7}	9.68×10^{-8}	1.19×10^{-7}
0.080	2.50×10^{-7}	2.26×10^{-7}	2.74×10^{-7}
0.085	5.61×10^{-7}	5.11×10^{-7}	6.13×10^{-7}
0.090	1.24×10^{-6}	1.14×10^{-6}	1.35×10^{-6}
0.095	2.75×10^{-6}	2.54×10^{-6}	2.96×10^{-6}
0.10	6.10×10^{-6}	5.69×10^{-6}	6.52×10^{-6}
0.12	1.30×10^{-4}	1.24×10^{-4}	1.36×10^{-4}
0.14	1.74×10^{-3}	1.66×10^{-3}	1.81×10^{-3}
0.16	1.50×10^{-2}	1.44×10^{-2}	1.56×10^{-2}
0.18	9.58×10^{-2}	9.23×10^{-2}	9.97×10^{-2}
0.20	4.86×10^{-1}	4.67×10^{-1}	5.06×10^{-1}
0.22	1.99×10^{0}	1.90×10^{0}	2.06×10^{0}
0.24	6.63×10^{0}	6.35×10^{0}	6.89×10^{0}
0.26	1.86×10^{1}	1.78×10^{1}	1.93×10^{1}
0.28	4.50×10^{1}	4.33×10^{1}	4.69×10^{1}
0.30	9.71×10^{1}	9.35×10^{1}	1.01×10^{2}
0.32	1.90×10^{2}	1.83×10^{2}	1.98×10^{2}
0.34	3.44×10^{2}	3.30×10^{2}	3.57×10^{2}
0.36	5.82×10^{2}	5.57×10^{2}	6.03×10^{2}
0.38	9.28×10^{2}	8.87×10^{2}	9.61×10^{2}
0.40	1.41×10^{3}	1.35×10^{3}	1.46×10^{3}
0.42	2.05×10^{3}	1.96×10^{3}	2.13×10^{3}
0.44	2.87×10^{3}	2.75×10^{3}	2.98×10^{3}
0.46	3.90×10^{3}	3.75×10^{3}	4.06×10^{3}
0.48	5.15×10^{3}	4.96×10^{3}	5.36×10^{3}
0.50	6.65×10^{3}	6.41×10^{3}	6.92×10^{3}
0.52	8.40×10^{3}	8.10×10^{3}	8.74×10^{3}
0.54	1.04×10^{4}	1.00×10^{4}	1.08×10^{4}
0.56	1.27×10^{4}	1.23×10^{4}	1.32×10^{4}
0.58	1.53×10^{4}	1.47×10^{4}	1.59×10^{4}
0.60	1.82×10^{4}	1.75×10^{4}	1.89×10^{4}
0.62	2.14×10^{4}	2.05×10^{4}	2.22×10^{4}
0.64	2.48×10^{4}	2.38×10^{4}	2.58×10^{4}
0.66	2.86×10^{4}	2.74×10^{4}	2.97×10^{4}
0.68	3.26×10^{4}	3.13×10^{4}	3.38×10^{4}
0.70	3.69×10^{4}	3.54×10^{4}	3.83×10^{4}
0.72	4.14×10^{4}	3.98×10^{4}	4.30×10^{4}
0.74	4.62×10^{4}	4.44×10^{4}	4.80×10^{4}
0.76	5.13×10^{4}	4.93×10^{4}	5.33×10^{4}
0.78	5.67×10^{4}	5.44×10^{4}	5.89×10^{4}
0.80	6.22×10^{4}	5.97×10^{4}	6.46×10^{4}
0.82	6.80×10^{4}	6.52×10^{4}	7.07×10^{4}
0.84	7.40×10^{4}	7.10×10^{4}	7.69×10^{4}
0.86	8.01×10^{4}	7.69×10^{4}	8.33×10^{4}
0.88	8.65×10^{4}	8.29×10^{4}	9.00×10^{4}
0.90	9.29×10^{4}	8.92×10^{4}	9.68×10^{4}
0.92	9.95×10^{4}	9.57×10^{4}	1.04×10^{5}
0.94	1.06×10^{5}	1.02×10^{5}	1.11×10^{5}
0.96	1.13×10^{5}	1.09×10^{5}	1.18×10^{5}
0.98	1.20×10^{5}	1.16×10^{5}	1.26×10^{5}
1.00	1.28×10^{5}	1.23×10^{5}	1.34×10^{5}

100 keV. Thus, we have determined the most precise rate for the $^{19}\mathrm{F}(p,\alpha\gamma)^{16}\mathrm{O}$ reaction to date. Now, the JUNA data provide greatly improved constraints on the $^{19}\mathrm{F}(p,\alpha\gamma)$ reaction rate for the temperature region down to 0.05 GK, which sufficiently covers the temperature range of interest for faint supernovae and AGB stars models [7,17].

As for the $^{19}\mathrm{F}(p,\alpha_0)^{16}\mathrm{O}$ channel, Fig. 7 shows the experimental data and *R*-matrix calculation of Lombardo *et al.* [28], and also the simple NACRE extrapolation [18] for comparison. It demonstrates that the $(p,\alpha\gamma)$ data are lower than those of (p,α_0) in the energy region of ≈50–200 keV. This implies that the (p,α_0) rate is higher than the $(p,\alpha\gamma)$ one in the relevant temperature region. Therefore, the present JUNA work provides strong experimental support that the (p,α_0) channel dominates the total (p,α) rate over a temperature region of ≈0.03–0.12 GK, and thus clarifies the role of these two channels.

V. SUMMARY

The present paper reports the detailed experimental results for the astrophysically important $^{19}\mathrm{F}(p,\alpha\gamma)^{16}\mathrm{O}$ reaction. The

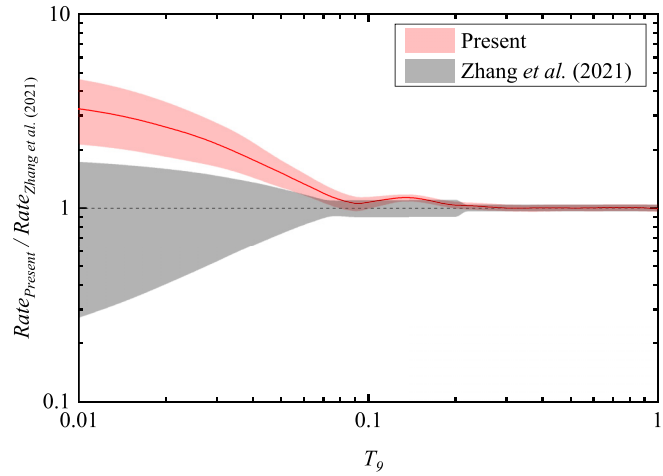

FIG. 9. Ratio of the present rate (based on the MCMC *R*-matrix fits) relative to that of Zhang *et al.* [38] (based on the general *R*-matrix fits).

measurement was directly reached down to the lowest energy region of $E_{\mathrm{c.m.}} \approx$ (72.4–344) keV. A low cross section down to the $\approx 10^{-12}$ b level was achieved relying on the extra-low background deep underground environment as well as the strong proton beam from JUNA facility. The astrophysical S factors have been obtained by R-matrix analysis together with a MCMC Bayesian uncertainty estimation. In the temperature region of astrophysical interest (0.05–1 GK), the precise thermonuclear $^{19}\mathrm{F}(p,\alpha\gamma)^{16}\mathrm{O}$ rate has been determined entirely based on solid experimental grounds, and is now sufficient for the requirement of astrophysics modeling.

Furthermore, this JUNA work strongly supports that the (p,α_0) channel dominates the total (p,α) rate over a temperature region of $\approx$0.03–0.12 GK based on the available knowledge of the (p,α_0) channel. However, a further direct measurement of this (p,α_0) channel below $\approx$180 keV (better, down to 70 keV) is still strongly suggested to verify the previous theoretical predictions or extrapolations.

ACKNOWLEDGMENTS

We wish to thank the staff of the CJPL and Yalong River Hydropower Development Company for logistics support. This work was financially supported by the National Natural Science Foundation of China (Grants No. 12075027, No. 11825504, No. 11961141004, and No. 11775133). R.J.D. utilized resources from the Notre Dame Center for Research Computing and R.J.D. and M.W. were supported by the National Science Foundation through Grant No. Phys-2011890, and the Joint Institute for Nuclear Astrophysics through Grant No. PHY-1430152 (JINA Center for the Evolution of the Elements). R.J.D. acknowledges useful discussions with Ivano Lombardo regarding R-matrix fitting for the ^{24}Mg system. D.K. acknowledges the support of the Romanian Ministry of Research and Innovation under research Contract No. 10N/PN 19 06 01 05. D.O. was supported by the National Science Foundation through Grant No. OAC-2004601.

[1] S. Lucatello, T. Masseron, J. A. Johnson, M. Pignatari, and F. Herwig, Astrophys. J. **729**, 40 (2011).
[2] D. Clayton, *Handbook of Isotopes in the Cosmos: Hydrogen to Gallium*, 1st ed. (Cambridge University Press, Cambridge, 2003)
[3] A. Renda *et al.*, Mon. Not. R. Astron. Soc. **354**, 575 (2004).
[4] S. E. Woosley and W. C. Haxton, Nature (London) **334**, 45 (1988).
[5] A. Jorissen, V. V. Smith, and D. L. Lambert, Astron. Astrophys. **261**, 164 (1992).
[6] M. Forestini, S. Goriely, A. Jorissen, and M. Arnould, Astron. Astrophys. **261**, 157 (1992).
[7] S. Cristallo *et al.*, Astrophys. J. **696**, 797 (2009).
[8] G. Meynet and M. Arnould, Astron. Astrophys. **355**, 176 (2000).
[9] C. Kobayashi *et al.*, Astrophys. J. Lett. **739**, L57 (2011).
[10] S. N. Shore *et al.*, Astron. Astrophys. **553**, A123 (2013).
[11] D. Kahl, J. José, and P. J. Woods, Astron. Astrophys. **653**, A64 (2021).
[12] M. Lugaro *et al.*, Astrophys. J. **615**, 934 (2004).
[13] S. Palmerini *et al.*, J. Phys.: Conf. Ser. **1308**, 012016 (2019).
[14] A. Frebel and J. E. Norris, Annu. Rev. Astron. Astrophys. **53**, 631 (2015).
[15] S. C. Keller *et al.*, Nature (London) **506**, 463 (2014).
[16] D. Ezer and A. G. W. Cameron, Astrophys. Space Sci. **14**, 399 (1971).
[17] O. Clarkson and F. Herwig, Mon. Not. R. Astron. Soc. **500**, 2685 (2020).
[18] C. Angulo *et al.*, Nucl. Phys. A **656**, 3 (1999).
[19] B. A. Watson, T. T. Bardin, J. A. Becker, and T. R. Fisher, Phys. Rev. Lett. **35**, 1333 (1975).
[20] I. Indelicato *et al.*, Astrophys. J. **845**, 19 (2017).
[21] I. Lombardo, D. Dell Aquila, J. J. He, G. Spadaccini, and M. Vigilante, Phys. Rev. C **100**, 044307 (2019).
[22] J. J. He *et al.*, Chin. Phys. C **42**, 015001 (2018).
[23] R. J. deBoer, O. Clarkson, A. J. Couture, J. Gorres, F. Herwig, I. Lombardo, P. Scholz, and M. Wiescher, Phys. Rev. C **103**, 055815 (2021).
[24] L. Y. Zhang, A. Y. López, M. Lugaro, J. J. He, and A. I. Karakas, Astrophys. J. **913**, 51 (2021).
[25] R. R. Betts, H. T. Fortune, and R. Middleton, Phys. Rev. C **11**, 19 (1975).
[26] M. Kious, Détermination de taux de réactions nucléaires conduisant á la nucléosynthèse stellaire du Fluor, Ph.D. thesis, Université de Paris-Sud, 1990 (unpublished).
[27] K. Spyrou *et al.*, Eur. Phys. J. A **7**, 79 (2000).
[28] I. Lombardo *et al.*, Phys. Lett. B **748**, 178 (2015).
[29] A. Couture *et al.*, Phys. Rev. C **77**, 015802 (2008).
[30] K. J. Kang *et al.*, J. Phys.: Conf. Ser. **203**, 012028 (2010).
[31] Y.-C. Wu *et al.*, Chin. Phys. C **37**, 086001 (2013).
[32] C. Broggini, D. Bemmerer, A. Guglielmetti, and R. Menegazzo, Annu. Rev. Nucl. Part. Sci. **60**, 53 (2010).
[33] Y. Shen *et al.*, Sci. China Phys. Mech. Astron. **60**, 102022 (2017).
[34] W. Liu *et al.*, Sci. China Phys. Mech. Astron. **59**, 642001 (2016).
[35] J. J. He *et al.*, Sci. China Phys. Mech. Astron. **59**, 652001 (2016).
[36] M. Wang, W. Huang, F. Kondev, G. Audi, and S. Naimi, Chin. Phys. C **45**, 030003 (2021).
[37] D. R. Tilley, H. R. Weller, and C. M. Cheves, Nucl. Phys. A **564**, 1 (1993).
[38] L. Y. Zhang *et al.*, Phys. Rev. Lett. **127**, 152702 (2021).
[39] Q. Wu *et al.*, Nucl. Instrum. Methods Phys. Res., Sect. A **830**, 214 (2016).
[40] L. Y. Zhang *et al.*, Nucl. Instrum. Methods Phys. Res., Sect. B **438**, 48 (2019).
[41] L. Y. Zhang *et al.*, Nucl. Instrum. Methods Phys. Res., Sect. B **496**, 9 (2021).
[42] J. Su *et al.* (unpublished).
[43] J. Su *et al.*, Sci. Bull. **67**, 125 (2022).
[44] S. Agostinelli *et al.*, Nucl. Instrum. Methods Phys. Res., Sect. A **506**, 250 (2003).
[45] A. Best *et al.*, Phys. Lett. B **797**, 134900 (2019).
[46] C. Iliadis, *Nuclear Physics of Stars* (Wiley-VCH, Weinheim, 2007).

[47] H. Becker, W. Kieser, C. Rolfs, H. Trautvetter, and M. Wiescher, Z. Phys. A **305**, 319 (1982).
[48] R. E. Azuma *et al.*, Phys. Rev. C **81**, 045805 (2010).
[49] E. Uberseder and R. J. deBoer, AZURE2 User Manual, 2015, https://azure.nd.edu.
[50] C. R. Brune, Phys. Rev. C **66**, 044611 (2002).
[51] D. Odell, C. R. Brune, D. R. Phillips, R. J. deBoer, and S. N. Paneru, Front. Phys. **10**, 888476 (2022).
[52] D. Foreman-Mackey, D. W. Hogg, D. Lang, and J. Goodman, Publ. Astron. Soc. Pac. **125**, 306 (2013).
[53] D. Foreman-Mackey, J. Open Source Softw. **1**, 24 (2016).
[54] C. E. Rolfsand W. S. Rodney, *Cauldrons in the Cosmos* (University of Chicago Press, Chicago, 1988).
[55] T. Rauscher and F.-K. Thielemann, At. Data Nucl. Data Tables **75**, 1 (2000).